INORGANIC CHEMISTRY FRONTIERS

RESEARCH ARTICLE

View Article Online
View Journal | View Issue

Cite this: *Inorg. Chem. Front.*, 2022, **9**, 3907

$[Pt_1Ag_{37}(SAdm)_{21}(Dppp)_3Cl_6]^{2+}$: intercluster transformation and photochemical properties†

Yaru Zhen,[a,b] Shan Jin,[c] Xi Kang,[a,b] Chang Xu,[a] Cao Fang,[a,b] Daqiao Hu *[a,b] and Manzhou Zhu *[a,b]

Received 19th May 2022,
Accepted 20th June 2022

DOI: 10.1039/d2qi01082h

rsc.li/frontiers-inorganic

Ligand-exchange-induced structure transformation has been exploited as an effective approach to dictate the size and structure of nanoparticles with atomic precision. However, phosphine ligand induced intercluster transformation remains rarely explored. Herein, we report the controllable preparation and the structural elucidation of a $[Pt_1Ag_{37}(SAdm)_{21}(Dppp)_3Cl_6]^{2+}$ nanocluster (Pt_1Ag_{37}; where Dppp is 1,3-bis (diphenyphosphino)propane and HSAdm is 1-adamantanethiol). Notably, the reaction of Pt_1Ag_{37} with PPh_3 triggers an intercluster transformation, giving rise to a stable and smaller-sized nanocluster, $[Pt_1Ag_{28}(SAdm)_{18}(PPh_3)_4]^{2+}$ (Pt_1Ag_{28}). Such an intercluster transformation is systematically monitored with ESI-MS and UV-vis. The photochemical properties of Pt_1Ag_{37} and Pt_1Ag_{28} nanoclusters are further investigated. Of note, in the presence of chiral Bdpp diphosphines (Bdpp = 2,4-bis-(diphenylphosphino) pentane), the enantiomeric $Pt_1Ag_{37}(SAdm)_{21}(R/S\text{-Bdpp})_3Cl_6$ ($R/S\text{-}Pt_1Ag_{37}$) are obtained, and such chiral nanoclusters displayed obvious optical activity. The results in this work hopefully shed light on the future preparation of metal nanoclusters for customized applications.

1 Introduction

Atomically precise metal nanoclusters are a class of molecular-like nanomaterials, which can be precisely manipulated with adjustable physicochemical properties at the atomic level.[1–11] Such nanoclusters have rich opportunities in both fundamental studies (*e.g.*, structure-dependent properties) and promising applications (*e.g.*, medicine, sensing, catalysis and energy).[7,12–15] Several efficient synthesis methods have been proposed to controllably prepare nanoclusters with molecular purity, including size focusing, ligand exchange, and intermolecular assembly.[16–21] Among them, the ligand exchange induced structure transformation (LEIST) is a highly versatile strategy for correlating the surface motifs/organic–metal interface with the reactivity of nanoclusters.[21–29] In the past decade, the LEIST of thiolated gold nanoclusters has been widely studied.[30–33] Jin *et al.* reported transformation of rod-like bicosahedral $Au_{38}(SCH_2CH_2Ph)_{24}$ to a tetrahedral $Au_{36}(TBBT)_{24}$ nanocluster.[34] The transformation from $Au_{23}(SCy)_{16}$ to $Au_{36}(TBBT)_{24}$ *via* $Au_{28}(TBBT)_{20}$ that activated by the presence of bulky 4-*tert*-butylbenzenethiol ligands was demonstrated by the Mandal group.[35] In addition, the transformations of alkynyl-protected gold nanoclusters have also been achieved. The Zang group reported the size conversion of a carboranealkynyl-protected gold nanocluster Au_{28} into a stable and smaller-sized nanocluster Au_{23}.[36] Indeed, the ligand exchange can be partial or complete, with or without altering the metallic kernel.

Nowadays, increasing interest is focused on the alloy nanoclusters with synergistic effect due to their potential for fundamental research.[8,37–39] With respect to silver-rich alloy nanoclusters, especially, for doping Pt heteroatoms into Ag nanoclusters that gives rise to Pt@Ag alloy nanoclusters, several research efforts have been made for investigating the structure–property correlations at the atomic level. Despite this, a limited number of Pt doping sliver-rich nanoclusters were reported, including $Pt_1Ag_{24}(SPhMe_2)_{18}$[40] protected by thiolates, $Pt_1Ag_{14}(SR)_6(PPh_3)_8$,[41] $Pt_1Ag_{24}(SR)_{16}(PPh_3)_3$,[42] Pt_1Ag_{26}(2-EBT)$_{18}(PPh_3)_6$,[18] Pt_1Ag_{28}(S-Adm)$_{18}(PPh_3)_4$ (Pt_1Ag_{28} for short),[43] $Pt_1Ag_{31}(SR)_{16}(DPPM)_3Cl_3$[44] coprotected by thiolates and phosphine ligands, $Pt_5Ag_{22}(C{\equiv}CPh)_{32}$,[45] $Pt_1Ag_{42}(C{\equiv}CPhMe)_{28}$,[46] stabilized by alkynyl, and so on. Among these nanoclusters, much effort has been devoted to the one-pot synthesis, such as $Pt_1Ag_{24}(SPhMe_2)_{18}$, $Pt_1Ag_{24}(SR)_{16}(PPh_3)_3$, Pt_1Ag_{26}(2-

[a]*Department of Chemistry and Centre for Atomic Engineering of Advanced Materials, Anhui Province Key Laboratory of Chemistry for Inorganic/Organic Hybrid Functionalized Materials, Anhui University, Hefei 230601, P. R. China. E-mail: hudaqiao@ahu.edu.cn, zmz@ahu.edu.cn*

[b]*Key Laboratory of Structure and Functional Regulation of Hybrid Materials of Ministry of Education, Anhui University, Hefei 230601, P. R. China*

[c]*Institutes of Physical Science and Information Technology, Anhui University, Hefei 230601, P. R. China*

†Electronic supplementary information (ESI) available: Fig. S1–S16 and Tables S1–S2. CCDC 2166689 for $Pt_1Ag_{37}(SAdm)_{21}(Dppp)_3Cl_6$. For ESI and crystallographic data in CIF or other electronic format see DOI: https://doi.org/10.1039/d2qi01082h

EBT)$_{18}$(PPh$_3$)$_6$, Pt$_5$Ag$_{22}$(C≡CPh)$_{32}$, and Pt$_1$Ag$_{42}$(C≡CPhMe)$_{28}$. Meanwhile, the ligand exchange strategy is a versatile approach to achieve Pt@Ag alloy nanoclusters with novel structures and distinct properties. For example, Pt$_1$Ag$_{28}$ was prepared by etching Pt$_1$Ag$_{24}$(SPhMe$_2$)$_{18}$ with both the HS-Adm and PPh$_3$ ligands[40] and when the Pt$_1$Ag$_{28}$ was reacted with Ag$_2$(Dppm)Cl$_2$, Pt$_1$Ag$_{31}$ was generated.[44] The fabrication of more Pt@Ag alloy nanoclusters is of great significance for further investigating the structure–property correlations in detail, rendering the future preparation of metal nanoclusters or cluster-based nanomaterials with customized structures and properties.

Herein, we report the synthesis of a [Pt$_1$Ag$_{37}$(SAdm)$_{21}$(Dppp)$_3$Cl$_6$]$^{2+}$ (denoted as Pt$_1$Ag$_{37}$) nanocluster co-protected by 1,3-bis(diphenyphosphino)propane (Dppp) and 1-adamantanethiol (HS-Adm) ligands. The phosphine ligand-exchange-induced structure transformation of Pt$_1$Ag$_{37}$ to [Pt$_1$Ag$_{28}$(SAdm)$_{18}$(PPh$_3$)$_4$]$^{2+}$ (denoted as Pt$_1$Ag$_{28}$) nanocluster was fulfilled in the presence of PPh$_3$. The intercluster conversion was monitored by ESI-MS and UV-vis absorption spectra. Furthermore, both Pt$_1$Ag$_{37}$ and Pt$_1$Ag$_{28}$ nanoclusters were emissive. Compared to Pt$_1$Ag$_{37}$, the photoluminescence (PL) lifetime of Pt$_1$Ag$_{28}$ was largely increased from 17.53 ns to 3.97 μs,[47] which might be attributed to different PL mechanism induced by different electronic structure in Pt$_1$Ag$_{37}$ and Pt$_1$Ag$_{28}$, respectively.[48] Additionally, chiral *R*/*S*-Pt$_1$Ag$_{37}$ nanoclusters were obtained *via* substituting achiral Dppp with homologous *R*/*S*-Bdpp ligands, which showed exciting CD activity and CPL response.

2 Experimental Methods

Chemicals

Hexachloroplatinic(IV) acid (H$_2$PtCl$_6$·6H$_2$O, 99.99%, metals basis), silver nitrate (AgNO$_3$, 99%, metals basis), 1-adamantanethiol (AdmSH, C$_{10}$H$_{16}$S, 99%), 1,3-bis(diphenyphosphino) propane (Dppp, 98%), triphenylphosphine (PPh$_3$, 99%), (2*S*,4*S*)-(−)-2,4-bis(diphenylphosphino)pentane ((2*S*,4*S*-Bdpp, purity 99%), (2*R*,4*R*)-(+)-2,4-bis(diphenylphosphino)pentane (2*R*,4*R*-Bdpp, purity 99%), tetraphenylboron sodium (NaBPh$_4$, 98%), and sodium borohydride (NaBH$_4$, 99.9%). Methylene chloride (CH$_2$Cl$_2$, HPLC), methanol (CH$_3$OH, HPLC), acetonitrileand (CH$_3$CN, HPLC) and *n*-hexane (Hex, HPLC grade).

Synthesis of the [Pt$_1$Ag$_{37}$(Dppp)$_3$(SAdm)$_{21}$Cl$_6$]$^{2+}$ nanocluster

AgNO$_3$ (60 mg, 0.36 mmol) was dissolved in 10 mL of CH$_3$OH and 2 mL CH$_3$CN under vigorous stirring. After 5 min, 1,3-bis (diphenyphosphino)propane (Dppp, 20 mg, 0.048 mmol) and 1-adamantane mercaptan (AdmSH, 30 mg, 0.178 mmol) were added. H$_2$PtCl$_6$·6H$_2$O (4 mg, 0.0075 mmol) was dissolved in 5 mL of CH$_3$OH and added to the reaction mixture. After half an hour, a freshly prepared sodium borohydride (NaBH$_4$, 20 mg, 0.14 mmol) was added to methanol solution of 50 μL of NEt$_3$. The solution changed from white to dark brown. This reaction lasted for 5 h at room temperature. The crude product was obtained by rotary evaporation and centrifugation 3 min at 11 000 rpm. The precipitate was washed with excess *n*-hexane and collected by centrifugation again. The crystals were crystallized from CH$_2$Cl$_2$/hexane at room temperature and afford red block crystals after 7 days. The yield was calculated as 14.6% based on the Pt element for Pt$_1$Ag$_{37}$.

Transformation from [Pt$_1$Ag$_{37}$(SAdm)$_{21}$(Dppp)$_3$Cl$_6$]$^{2+}$ to [Pt$_1$Ag$_{28}$(SAdm)$_{18}$(PPh$_3$)$_4$]$^{2+}$

5 mg of [Pt$_1$Ag$_{37}$(SAdm)$_{21}$(Dppp)$_3$Cl$_6$]$^{2+}$ (0.5 μmol) was dissolved in 15 mL of CH$_2$Cl$_2$, to which solution the PPh$_3$ ligand (5.2 mg, 20 μmol) was added. The reaction was allowed to proceed for 360 min at room temperature. Time-dependent UV-vis and ESI-MS spectra were monitored.

Synthesis of the chiral Pt$_1$Ag$_{37}$(SAdm)$_{21}$(*R*/*S*-Bdpp)$_3$Cl$_6$ nanocluster

Chiral Pt$_1$Ag$_{37}$ (SAdm)$_{21}$(*R*/*S*-Bdpp)$_3$Cl$_6$ nanocluster was obtained referring to the preparation of Pt$_1$Ag$_{37}$(SAdm)$_{21}$(Dppp)$_3$Cl$_6$, using 18 mg (2*S*,4*S*-Bdpp)/(2*R*,4*R*-Bdpp) in place of 20 mg of Dppp. All the other experimental conditions were kept unchanged.

Fitting of dynamic curves

All the dynamic curves in this study were fitted with the exponential decay function:

$$y = Ae^{(-x)/\tau} + y_0,$$

where x is the reaction time and y is variation of the absorbance at 408 nm of Pt$_1$Ag$_{37}$, the ratio of C_0 and C_t (the concentration of Pt$_1$Ag$_{37}$ at time 0 min and t min) was determined by the relative absorbance at time 0 min (A_0) and time t min (A_t). τ is the lifetime of the curve and $\tau \ln 2$ is the half-life ($T_{1/2}$).

DFT calculations

The structures of PtAg nanocluster is fully optimized by using density functional theory (DFT) method at B3LYP/def2SVP[49,50] level of theory with Grimme D3 corrections[51] and verified to be true minima by frequency check. The cubane groups in the ligands of synthesized cluster are replaced by CH$_3$ groups in order to reduce the computational cost. UV absorption simulations are performed at the same level by time-dependent density functional theory (TD-DFT)[52,53] method. All calculations are carried out in Gaussian 16[54] and Multiwfn[55] package, and the Kohn–Sham orbitals are visualized in the Chemcraft program.[56]

Characterization

All UV-vis spectra of the nanoclusters were recorded using an Agilent 8453, and the samples were dissolved in CH$_2$Cl$_2$ whose background correction was made using a CH$_2$Cl$_2$ blank. Thermogravimetric analysis (TGA) was carried out using a thermogravimetric analyzer (DTG-60H, Shimadzu Instruments, Inc.) with 5 mg of the nanocluster in a SiO$_2$ pan at a heating rate of 10 K min^{-1} from 323 to 1073 K. X-ray photoelectron spectroscopy (XPS) measurements were performed using a Thermo ESCALAB 250 configured with a monochromated Al

Kα (1486.8 eV) 150 W X-ray source, 0.5 mm circular spot size, a flood gun to counter charging effects, and an analysis chamber base pressure lower than 1×10^{-9} mbar, and the data were collected with FAT of 20 eV. Electrospray ionization time-of-flight mass spectrometry (ESI-TOF-MS) measurements were performed on a MicrOTOF-QIII high-resolution mass spectrometer. Photoluminescence spectra were measured using a HORIBA FluoroMax+ spectrofluorometer with the same optical density (OD) of ~0.05. Absolute quantum yields were measured with dilute solutions of nanoclusters (0.05 OD absorption at 410 nm) on a HORIBA FluoroMax+. Transmission electron microscopy (TEM) was conducted on a JEM-2100 microscope with an accelerating voltage of 200 kV. Data collection for single crystal X-ray diffraction was carried out using a Stoe Stadivari diffractometer under a liquid nitrogen flow at 170 K, using graphite-monochromatized Cu Kα radiation (λ = 1.54186 Å). Data reductions and absorption corrections were performed using SAINT and SADABS programs, respectively. CD spectra were recorded with a BioLogic MOS-500 CD spectropolarimeter in a 0.1 cm path length quartz cell. The spectra were recorded in diluted solutions of dichloromethane and the signal of the blank solvent was subtracted. PL intensity and polarization spectra were measured on a JASCO CPL-300 circularly polarized luminescence spectrophotometer.

3 Results and discussion

Synthesis and characterization of Pt_1Ag_{37} nanocluster

The Pt_1Ag_{37} nanocluster was synthesized *via* a one-pot procedure. Red block crystals were obtained after the cultivation in DCM/Hex for seven days (Fig. S1a†). TEM image showed that the Pt_1Ag_{37} was uniform with an average size of 1.69 nm (Fig. S1b†). The UV-vis spectra of Pt_1Ag_{37} in CH_2Cl_2 displayed two strong peaks centered at 408 nm and 475 nm, and two weak shoulder peaks at 327 and 435 nm, in good agreement with the time-dependent density functional theory (TDDFT) calculated spectrum (Fig. 1a). Based on computed excitation energies and Kohn–Sham (KS) orbitals, we further assigned the orbital transition modes of four distinct absorption peaks which were shown in Fig. S2.† To verify the formula of Pt_1Ag_{37}, the electrospray ionization mass spectrometry (ESI-MS) was performed that showed an intense peak at *m*/*z* of 4574.8 Da, corresponding to the characteristic peak of $[Pt_1Ag_{37}(SAdm)_{21}(Dppp)_3Cl_6]^{2+}$ (Fig. 1b), with a weak peak at 3891.16 Da corresponding to the $[Pt_1Ag_{32}(SAdm)_{16}(Dppp)_2Cl_6(CH_2Cl_2)_4(CH_3CN)_2]^{2+}$, with a loss of Ag_5S_5 motif and one Dppp ligand of Pt_1Ag_{37}. The experimental isotopic distributions matched perfectly with the simulation model. The free electron count of Pt_1Ag_{37} was calculated as 8*e* (*i.e.*, 37 (Ag)-21 (SR)-6 (Cl)-2 (charge) = 8*e*), the same as that of the reported $Pt_1Ag_{24}(SR)_{16}(PPh_3)_3$,[42] $Pt_1Ag_{26}(2\text{-EBT})_{18}(PPh_3)_6$,[18] and $Pt_1Ag_{28}(SAdm)_{18}(PPh_3)_4$[43] nanoclusters. The X-ray photoelectron spectroscopy (XPS) result revealed the presence of Pt, Ag, P, Cl, C and S in the nanocluster (Fig. 1c). An expanded view of the Pt 4f spectrum showed two peaks centered at 71.08 eV and 74.41 eV, corresponding to characteristic peaks of Pt $4f_{7/2}$ and Pt $4f_{5/2}$ for Pt^0, respectively (Fig. S3†).[57,58] Thermogravimetric analysis (TGA) was also performed with a total weight loss of 53.94 wt% (Fig. 1d), consistent with the theoretical loss of 54.24 wt%. The Pt_1Ag_{37} nanocluster exhibit good thermal stability, because no decomposition was observed when stored in CH_2Cl_2 for two days (Fig. S4†).

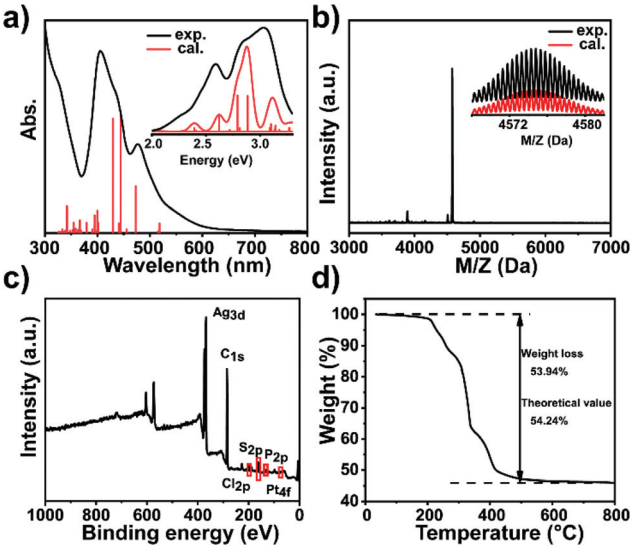

Fig. 1 (a) Experimental UV–vis spectrum of Pt_1Ag_{37} (black) and its excitation energies calculated by TD-DFT (red). Inset: The corresponding UV–vis data on the energy scale; the red curve was constructed *via* Lorentzian broadening of 0.1 eV. (b) ESI-MS result in a positive mode. (c) XPS, and (d) TGA results of Pt_1Ag_{37}.

Atomic structure

The detailed structure of Pt_1Ag_{37} could be divided into two parts, including the metal kernel and the stabilizing shell. The icosahedral kernel, *i.e.*, Pt_1Ag_{12}, was stabilized by a shell including three $Ag_3(SR)_2Cl_2$ motifs connected *via* an Ag bridge, three $Ag_5(SR)_5$ motifs, and three Dppp motifs (Fig. 2). Besides, the whole $Ag@(Ag_3(SR)_2Cl_2\text{-}Ag_5(SR)_5\text{-}Dppp)_3$ shell with a C_3 symmetry was bound onto the icosahedral kernel (Fig. S5†). From the other side, the whole trefoil-like shell was constituted of three leave-like units connected by one Ag atom. In Pt_1Ag_{37}, the bond lengths between the central Pt and the icosahedron-shell Ag atoms varied from 2.735 to 2.789 Å, with an average distance of 2.752 Å. The Ag–Ag bond lengths ranged from 2.805 to 2.956 Å (averagely, 2.895 Å). Additionally, the remaining six Cl atoms linked to six silver atoms, and the average bond length of Ag–Cl was 2.506 Å. The P atoms of phosphine ligands were also directly attached to Ag atoms with an average bond length of 2.407 Å (Fig. S6†).

Transformation from Pt_1Ag_{37} to Pt_1Ag_{28}

The reaction between Pt_1Ag_{37} with 40-equivalent of PPh_3 gave rise to the generation of a smaller reprted nanocluster, $Pt_1Ag_{28}(S\text{-}Adm)_{18}(PPh_3)_4$,[43] fulfilling the ligand exchange

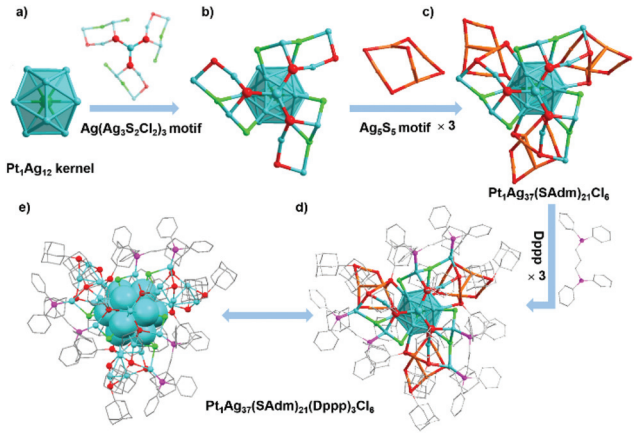

Fig. 2 (a) Pt_1Ag_{12} kernel; (b) $Pt_1Ag_{12}@Ag(Ag_3S_2Cl_2)_3$ motifs; (c) $Pt_1Ag_{12}@Ag(Ag_3S_2Cl_2)_3@(Ag_5S_5)_3$ motifs. (d) The total structure of ball-stick and (e) the space-fill pattern of Pt_1Ag_{37}. Color labels: dark green, Pt; blue, orange, Ag; green, Cl; red, S; magenta, P; gray, C.

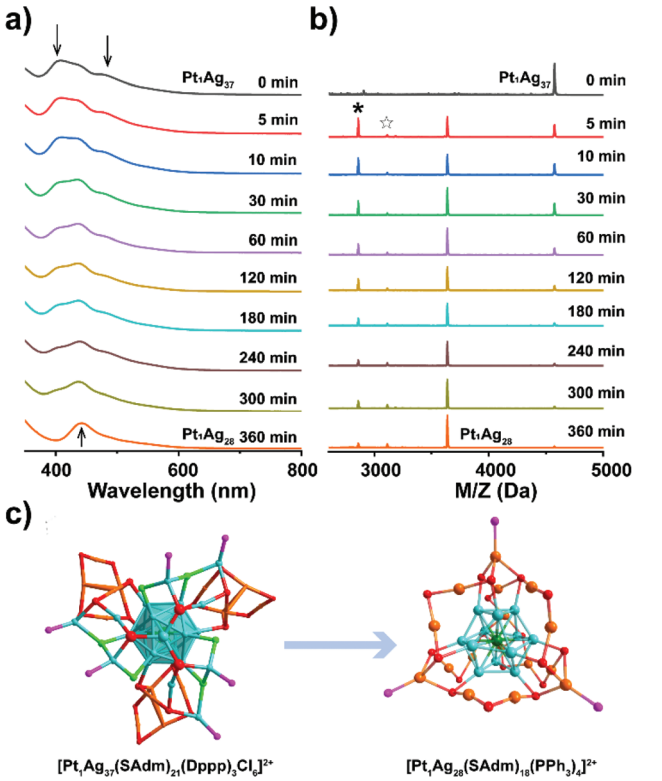

Fig. 3 (a) Time-dependent UV-vis and (b) ESI-MS results of the intercluster transformation from Pt_1Ag_{37} to Pt_1Ag_{28}. ☆ and * may be identified as intermediates (*i.e.* $[Pt_1Ag_{25}(SAdm)_{15}(Dppp)_2]^{2+}$ and $Ag_8(SAdm)_7(Dppp)_2$, separately). (c) Intercluster transformation from Pt_1Ag_{37} to Pt_1Ag_{28}. Color labels: dark green, Pt; blue, orange, Ag; green, Cl; red, S; magenta, P.

induced intercluster transformation. The intercluster transformation was monitored by UV-vis and ESI-MS. According to time-dependent UV-vis spectra (Fig. 3a), the peaks at 408 and 475 nm displayed the characteristic feature of Pt_1Ag_{37} at 0 min. After 5 min, a new peak located at 440 nm corresponding to the Pt_1Ag_{28} nanocluster appeared.[43] At t = 10 min to 300 min, the peaks at 408 and 475 attenuated gradually accompanied by the increase of the peak at 440 nm. After 6 hours, the peaks at 408 and 475 nm disappeared, demonstrating the complete intercluster transformation from Pt_1Ag_{37} into Pt_1Ag_{28}. The DFT calculation results revealed a larger HOMO–LUMO energy gap for Pt_1Ag_{37} relative to Pt_1Ag_{28} (2.64 eV *versus* 1.76 eV; Fig. S7†), agreeing with an inverse-proportion trend to size, similar to those of Pt_1Ag_{31} and Pt_1Ag_{28} (1.92 eV *versus* 1.76 eV).[44]

Concurrently, the time-dependent ESI-MS clearly showed ligand exchange on the Pt_1Ag_{37} nanocluster along with the intercluster transformation (Fig. 3b). At the initial stage, the Pt_1Ag_{37} nanocluster displayed an intense peak at 4574.8 Da. After 5 min, the peak at 4574.8 Da decreased with a new peak emerged at 3637.67 Da, corresponding to the Pt_1Ag_{28} nanocluster (Fig. S8b†). Meanwhile, two new peaks with different intensities centered at 3113.12 Da and 2859.17 Da were observed, which may be identified as intermediates (*i.e.* $[Pt_1Ag_{25}(SAdm)_{15}(Dppp)_2]^{2+}$ and $Ag_8(SAdm)_7(Dppp)_2$, separately) during the ligand exchange process. As the reaction continued, the intensity of the Pt_1Ag_{28} peak increased, while the intensity of these Pt_1Ag_{37} and intermediates decreased (Fig. 3b, t = 10 and 300 min profiles). After 6 h, the mass peak of Pt_1Ag_{37} disappeared, suggesting a complete intercluster transformation from Pt_1Ag_{37} to Pt_1Ag_{28}. It is worth mentioning that with different equivalent of PPh_3 ligand, the ligand exchange process proceeded in different ways (Fig. S9†). With the addition of 20 equivalent of PPh_3, the reaction proceeded in the same way but with different conversion rate compared with 40 equivalent of PPh_3 during the first 60 min. After that, the peak of Pt_1Ag_{37} and Pt_1Ag_{28} decreased simultaneously accompanied by the emergence of new fragment peaks at the range of 3000–3500 Da, indicating the disassociation of both Pt_1Ag_{37} and Pt_1Ag_{28}. At t = 360 min, the peaks of Pt_1Ag_{37} and Pt_1Ag_{28} disappeared completely. When the PPh_3 ligand was increased to 60 equivalent, the reaction completed within 180 min without the appearance of intermediate peaks at the range of 2500 Da–4000 Da. The 408 nm of peak UV-vis spectra could be used for the kinetic study. After analyzing the fitting coefficients of the functions.[59] the half-life periods ($T_{1/2}$) of reaction with 40 and 60 equivalent of PPh_3 were calculated and compared, showing a sequence as 60 eq. (27.43 min) < 40 eq. (38.71 min) (Fig. S10†).

The Pt_1Ag_{37} and Pt_1Ag_{28} displayed significantly different structures. Along with the intercluster transformation, the icosahedral Pt_1Ag_{12} kernel of Pt_1Ag_{37} was converted into a face-centered cubic (FCC) Pt_1Ag_{12} kernel in Pt_1Ag_{28} (Fig. 3c). Besides, the surface shell was changed from three $Ag_8(SR)_7Cl_2Dppp$ trefoil-like motifs to four $Ag_4(SR)_6(PPh_3)_1$ cage-like motifs by sharing the terminal thiol ligands, among which the vertex Dppp ligands on Pt_1Ag_{37} were peeled off. The difference in bond lengths was also observed and compared. The Pt–Ag average bond length (2.752 Å) in the Pt_1Ag_{37} kernel was shorter than that of Pt_1Ag_{28} (2.783 Å), suggesting the more robust Pt–Ag bond in Pt_1Ag_{37} (Table S1†). Besides, the Ag

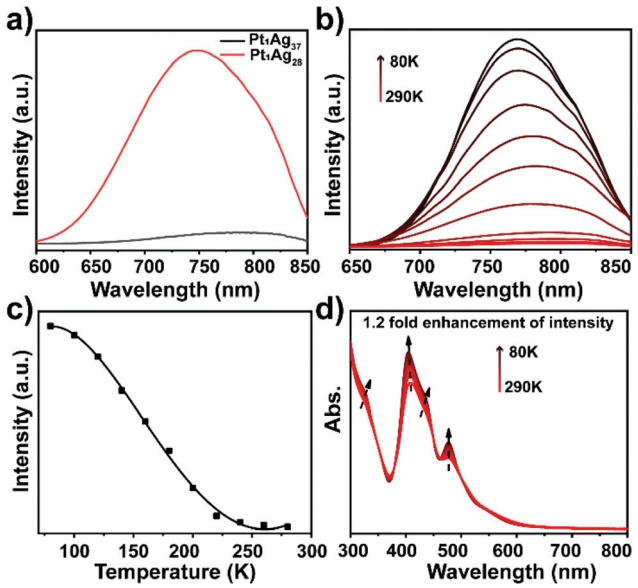

Fig. 4 (a) PL of the Pt_1Ag_{37} and Pt_1Ag_{28} nanoclusters at room temperature. (b) Temperature-dependent PL spectra of Pt_1Ag_{37} nanocluster in CH_2Cl_2. (c) Variation of the PL Intensity over temperature. (d) Temperature-dependent UV-vis absorption of Pt_1Ag_{37} in CH_2Cl_2.

(kernel)–S(motif) and Ag(motif)–S(motif) bonds in Pt_1Ag_{37} were also shorter than those of Pt_1Ag_{28}. However, the Ag–Ag bonds of the icosahedral (averagely, 2.895 Å) and Ag(motif)–P (motif) (averagely, 2.407 Å) bonds in Pt_1Ag_{37} were much longer than those in Pt_1Ag_{28}. The average distance between the terminal Ag and kernel Ag atom in Pt_1Ag_{12} of Pt_1Ag_{37} was 6.961 Å, much longer than that in Pt_1Ag_{28} (4.290 Å), which was attributed to the bulky peripheral ligands of Pt_1Ag_{37}. The transformation of the outermost shell further caused a change towards the core–shell interaction, which altered the innermost Pt_1Ag_{12} kernel from an icosahedral configuration of Pt_1Ag_{37} to a FCC configuration of Pt_1Ag_{28}.

Photoluminescent property

The photoluminescence (PL) spectra of Pt_1Ag_{37} and Pt_1Ag_{28} was analyzed and compared (Fig. 4a). The excitation spectrum of Pt_1Ag_{37} nanocluster was shown in Fig. S11.† Upon excitation at 410 nm, the Pt_1Ag_{37} nanocluster (in CH_2Cl_2 solution) emits at 789 nm, with a PL quantum yield (QY) of 1.49%. By comparison, the Pt_1Ag_{28} nanocluster emits at 747 nm with a higher PL QY of 4.9% upon excitation at 360 nm.‡ [43] Moreover, the PL lifetime of Pt_1Ag_{37} was 17.53 ns measured by time-correlated single-photon counting (TCSPC) (Fig. S12†), whereas that for Pt_1Ag_{28} was determined as 3.97 μs.[47] Such a PL enhancement may be attributed to the different PL mechanism induced by different electronic structure in Pt_1Ag_{37} and Pt_1Ag_{28}, respectively (Fig. S7†). Specifically, the LUMO density of Pt_1Ag_{37} was concentrated mainly on Ag core structures, while the HOMO density distributed over the metal core and SR motif structures. In this context, the PL of Pt_1Ag_{37} might originate from the metal-to-metal-to-ligand charge transfer (MMLCT) process.[48] For Pt_1Ag_{28}, the PL was ascribed to ligand-to-metal charge transfer (LMCT) based on the excited state behavior analysis.[43] The temperature-dependent fluorescence of Pt_1Ag_{37} in CH_2Cl_2 was also monitored, showing a 37.5-fold enhancement on the PL intensity along with the temperature-lowering process from 290 to 80 K and a bule-shifted emission from 789 to 768 nm (Fig. 4b and c). The increase of the fluorescence intensity may result from the restriction of intramolecular vibration as the temperature decreased.[60] Meanwhile, the red-shift of PL peak may be ascribed to the decreased molecular transition energy as the temperature increased. The temperature dependent optical absorption of Pt_1Ag_{37} in CH_2Cl_2 was further investigated and a 1.2-fold enhancement of the peaks at 408 and 475 nm was shown in the corresponding temperature-lowering process (Fig. 4d). Additionally, two new peaks locating at 327 and 435 nm appeared and enhanced gradually in the cooling process. Accordingly, the PL QY of the Pt_1Ag_{37} nanocluster at 80 K was enhanced from 1.49% to 46.56% (1.49% × 37.5/1.2 = 46.56%) during the temperature-lowering process.

Optical activity

Compared with the monodentate ligand PPh_3 for Pt_1Ag_{28}, the bidentate ligand Dppp for Pt_1Ag_{37} shows more opportunities to functionalizing nanoclusters. By controlling the enantioselectivity of the peripheral Dppp ligand, the enantioselective synthesis of optically pure intrinsic chiral Pt_1Ag_{37} nanocluster could be achieved. The chiral ligands (2*S*,4*S*)-2,4-bis(diphenylphosphino) pentane (2*S*,4*S*-Bdpp) and (2*R*,4*R*)-2,4-bis(diphenylphosphino) pentane (2*R*,4*R*-Bdpp) were exploited to substitute the achiral Dppp ligand in the nanocluster synthesis. The UV-vis spectra of the racemic Pt_1Ag_{37} and *R*/*S*-Pt_1Ag_{37} nanoclusters in CH_2Cl_2 were measured. As shown in Fig. 5a, the racemic Pt_1Ag_{37} and two enantiomers *R*/*S*-Pt_1Ag_{37} nanoclusters exhibited two strong bands at 405 and 482 nm, demonstrating their similar geometric and electronic compositions and structures. ESI-MS results demonstrated that two peaks, corresponding to $[Pt_1Ag_{32}(SAdm)_{16}(Bdpp)_3Cl_6]^{3+}$ and $[Pt_1Ag_{32}(SAdm)_{16}(Bdpp)_3Cl_7]^{2+}$ with a loss of an Ag_5S_5 motif, were detected (Fig. 5b and Fig. S13†).

Significantly, compared with the optically inactive Pt_1Ag_{37}, the newly obtained *R*/*S*-Pt_1Ag_{37} nanoclusters displayed apparently optical activity. The circular dichroism (CD) spectra of the *R*/*S*-Pt_1Ag_{37} solutions exhibited mirror-images signals around 250, 287, 326, 355, 401, 476, and 501 nm (Fig. 5c). The anisotropy factors $g = \Delta A/A = \theta[\mathrm{mdeg}]/(32\,980 \times A)$ were calcu-

‡In our previous works, the photoluminescence of $Pt_1Ag_{28}(SR)_{18}(PR')_4$ was characterized using an instrument of HITACHI (F-7000) with a photoluminescence detection limit at 750 nm, which resulted in an inaccurate emission wavelength (*i.e.*, 672 nm). In this work, we tested the PL of nanoclusters by an instrument of HORIBA Scientific (FluoroMax+) with a higher photoluminescence detection limit at 870 nm. And here, we updated the emission wavelength data of $Pt_1Ag_{28}(S\text{-}Adm)_{18}(PPh_3)_4$ to 747 nm. The photoluminescence quantum yields and emission lifetimes were correct in previous works since they were detected by an instrument of HORIBA Scientific (FluoroMax-4P) with a photoluminescence detection limit at 870 nm.

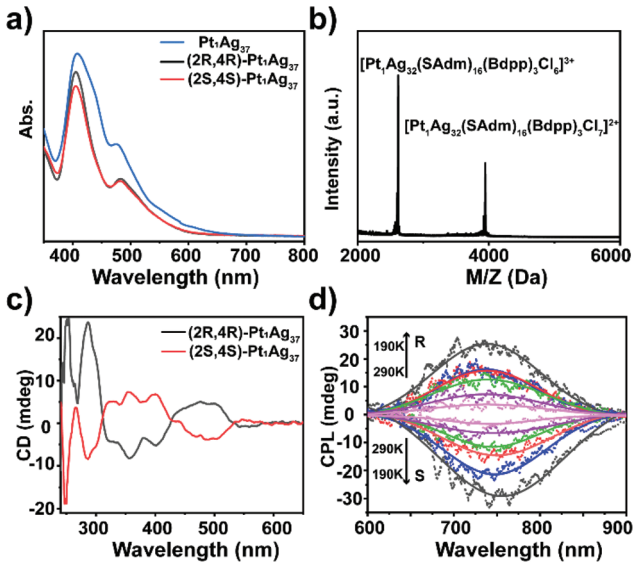

Fig. 5 (a) UV-vis spectra of *R*/*S*-Pt_1Ag_{37} and Rac-Pt_1Ag_{37}. (b) ESI-MS spectra of *S*-Pt_1Ag_{37} in CH_2Cl_2. CD (c) and temperature-dependent CPL spectra (d) of the enantiomers.

lated, and the maximum anisotropy factor was up to 7.0×10^{-4} at 501 nm (Fig. S14a†). Furthermore, the CD spectra of pure *R*/*S*-Bdpp ligands were quite different from that of *R*/*S*-Pt_1Ag_{37} (Fig. S15†). These results demonstrated that the CD signals of *R*/*S*-Pt_1Ag_{37} originated from the nanoclusters but not the free ligands, confirming the chirality of *R*/*S*-Pt_1Ag_{37}. The temperature-dependent circularly polarized luminescence (CPL) signals were then collected (Fig. 5d). The *R*/*S*-Pt_1Ag_{37} performed obvious CPL responses that corresponded to their emission bands (600–900 nm) (Fig. S16†). Besides, the intensity of CPL signals significantly enhanced with the temperature drop process from 290 to 190 K, consistent with variation of the absorption and emission of such nanoclusters. The calculated g_{lum} values were all at the level of 10^{-3} (Fig. S14b†) with a highest g_{lum} value of $\pm 2 \times 10^{-3}$ at about 887 nm.

4 Conclusions

In summary, we synthesized a Pt_1Ag_{37} nanocluster *via* a one-pot method, and operated the phosphine ligand exchange-induced intercluster transformation from Pt_1Ag_{37} to Pt_1Ag_{28}. The UV-vis and ESI-MS were performed to track the intercluster transformation. Structurally, the Pt_1Ag_{37} nanocluster contained an icosahedral Pt_1Ag_{12} kernel, in contrast to the FCC Pt_1Ag_{12} kernel of the Pt_1Ag_{28} nanocluster. Besides, these two Pt@Ag nanoclusters presented significantly different surface motif structures. A 3.3-fold enhancement on PL QY was accomplished *via* the ligand exchange from Pt_1Ag_{37} to Pt_1Ag_{28}. Furthermore, chiral *R*/*S*-Ag_{37} nanoclusters enantiomers could be obtained by substituting achiral Dppp into chiral bidentate phosphine ligands. The chiral *R*/*S*-Ag_{37} nanoclusters displayed obvious optical activity. Our results suggest that the phosphine ligand exchange can be exploited as an efficient approach to fulfill the size evolution and fluorescence regulation of metal nanoclusters, and hopefully contributes more to the fabrication of noble metal nanoclusters, for potential biological, electronic and catalytic applications.

Author contributions

Y. Z. carried out experiments, analyzed the data and wrote the manuscript. X. K. revised the manuscript and C. X. completed DFT calculations. S. J. assisted the X-ray structure analysis. C. F. assisted the measurements of UV-vis and ESI-MS. M. Z. and D. H. designed the project, analyzed the data, and revised the manuscript.

Conflicts of interest

There are no conflicts to declare.

Acknowledgements

The authors acknowledge the financial support by NSFC (21631001, 21871001, and 91961121), the Ministry of Education, and the University Synergy Innovation Program of Anhui Province (GXXT-2020-053).

References

1 R. Jin, G. Li, S. Sharma, Y. Li and X. Du, Toward Active-Site Tailoring in Heterogeneous Catalysis by Atomically Precise Metal Nanoclusters with Crystallographic Structures, *Chem. Rev.*, 2021, **121**, 567–648.
2 J. Yan, B. K. Teo and N. Zheng, Surface Chemistry of Atomically Precise Coinage–Metal Nanoclusters: From Structural Control to Surface Reactivity and Catalysis, *Acc. Chem. Res.*, 2018, **51**, 3084–3093.
3 X. Kang and M. Zhu, Intra-cluster growth meets inter-cluster assembly: The molecular and supramolecular chemistry of atomically precise nanoclusters, *Coord. Chem. Rev.*, 2019, **394**, 1–38.
4 Q. Tang, G. Hu, V. Fung and D.-E. Jiang, Insights into Interfaces, Stability, Electronic Properties, and Catalytic Activities of Atomically Precise Metal Nanoclusters from First Principles, *Acc. Chem. Res.*, 2018, **51**, 2793–2802.
5 Y. Jin, C. Zhang, X.-Y. Dong, S.-Q. Zang and T. C. W. Mak, Shell engineering to achieve modification and assembly of atomically-precise silver clusters, *Chem. Soc. Rev.*, 2021, **50**, 2297–2319.
6 Z. Liu, Z. Wu, Q. Yao, Y. Cao, O. J. H. Chai and J. Xie, Correlations between the fundamentals and applications of ultrasmall metal nanoclusters: Recent advances in catalysis and biomedical applications, *Nano Today*, 2021, **36**, 101053.

7 A. Fernando, K. L. D. M. Weerawardene, N. V. Karimova and C. M. Aikens, Quantum Mechanical Studies of Large Metal, Metal Oxide, and Metal Chalcogenide Nanoparticles and Clusters, *Chem. Rev.*, 2015, **115**, 6112–6216.
8 Q. Yao, X. Yuan, T. Chen, D. T. Leong and J. Xie, Engineering Functional Metal Materials at the Atomic Level, *Adv. Mater.*, 2018, **30**, 1802751.
9 I. Chakraborty and T. Pradeep, Atomically Precise Clusters of Noble Metals: Emerging Link between Atoms and Nanoparticles, *Chem. Rev.*, 2017, **117**, 8208–8271.
10 P. Chakraborty, A. Nag, A. Chakraborty and T. Pradeep, Approaching Materials with Atomic Precision Using Supramolecular Cluster Assemblies, *Acc. Chem. Res.*, 2019, **52**, 2–11.
11 W. Kurashige, Y. Niihori, S. Sharma and Y. Negishi, Precise synthesis, functionalization and application of thiolate-protected gold clusters, *Coord. Chem. Rev.*, 2016, **320–321**, 238–250.
12 G. Li and R. Jin, Atomically Precise Gold Nanoclusters as New Model Catalysts, *Acc. Chem. Res.*, 2013, **46**, 1749–1758.
13 P. Zhang, X-ray Spectroscopy of Gold–Thiolate Nanoclusters, *J. Phys. Chem. C*, 2014, **118**, 25291–25299.
14 W. Kurashige, Y. Niihori, S. Sharma and Y. Negishi, Recent Progress in the Functionalization Methods of Thiolate-Protected Gold Clusters, *J. Phys. Chem. Lett.*, 2014, **5**, 4134–4142.
15 Y. Yu, Q. Yao, Z. Luo, X. Yuan, J. Y. Lee and J. Xie, Precursor engineering and controlled conversion for the synthesis of monodisperse thiolate-protected metal nanoclusters, *Nanoscale*, 2013, **5**, 4606–4620.
16 M. S. Bootharaju, C. P. Joshi, M. R. Parida, O. F. Mohammed and O. M. Bakr, Templated Atom-Precise Galvanic Synthesis and Structure Elucidation of a $[Ag_{24}Au(SR)_{18}]^-$ Nanocluster, *Angew. Chem., Int. Ed.*, 2016, **55**, 922–926.
17 H. Wu, Y.-G. Fang, R. Anumula, G. N. Andrew, G. Cui, W. Fang, Z. Luo and J. Yao, A mono-copper doped undeca-gold cluster with up-converted and anti-stokes emissions of fluorescence and phosphorescence, *Nanoscale*, 2021, **13**, 5300–5306.
18 L. He, J. Yuan, N. Xia, L. Liao, X. Liu, Z. Gan, C. Wang, J. Yang and Z. Wu, Kernel Tuning and Nonuniform Influence on Optical and Electrochemical Gaps of Bimetal Nanoclusters, *J. Am. Chem. Soc.*, 2018, **140**, 3487–3490.
19 J. Lin, W. Li, C. Liu, P. Huang, M. Zhu, Q. Ge and G. Li, One-phase controlled synthesis of Au_{25} nanospheres and nanorods from 1.3 nm Au : PPh_3 nanoparticles: the ligand effects, *Nanoscale*, 2015, **7**, 13663–13670.
20 C. A. Hosier and C. J. Ackerson, Regiochemistry of Thiolate for Selenolate Ligand Exchange on Gold Clusters., *J. Am. Chem. Soc.*, 2019, **141**, 309–314.
21 Z. Wu, Q. Yao, S. Zang and J. Xie, Directed Self-Assembly of Ultrasmall Metal Nanoclusters, *ACS Mater. Lett.*, 2019, **1**, 237–248.
22 M.-M. Xu, Q. Chen, L.-H. Xie and J.-R. Li, Exchange reactions in metal-organic frameworks: New advances, *Coord. Chem. Rev.*, 2020, **421**, 213421.
23 Y. Niihori, S. Hossain, B. Kumar, L. V. Nair, W. Kurashige and Y. Negishi, Perspective: Exchange reactions in thiolate-protected metal clusters, *APL Mater.*, 2017, **5**, 053201.
24 X. Kang and M. Zhu, Transformation of Atomically Precise Nanoclusters by Ligand-Exchange, *Chem. Mater.*, 2019, **31**, 9939–9969.
25 C. A. Mirkin, R. L. Letsinger, R. C. Mucic and J. J. Storhoff, A DNA-based method for rationally assembling nanoparticles into macroscopic materials, *Nature*, 1996, **382**, 607–609.
26 C. K. Kim, P. Ghosh, C. Pagliuca, Z.-J. Zhu, S. Menichetti and V. M. Rotello, Entrapment of Hydrophobic Drugs in Nanoparticle Monolayers with Efficient Release into Cancer Cells, *J. Am. Chem. Soc.*, 2009, **131**, 1360–1361.
27 Y. Negishi, H. Horihata, A. Ebina, S. Miyajima, M. Nakamoto, A. Ikeda, T. Kawawaki and S. Hossain, Selective formation of $[Au_{23}(SPhtBu)_{17}]^0$, $[Au_{26}Pd(SPhtBu)_{20}]^0$ and $[Au_{24}Pt(SC_2H_4Ph)_7(SPhtBu)_{11}]^0$ by controlling ligand-exchange reaction, *Chem. Sci.*, 2022, **13**, 5546–5556.
28 S. Gratious, A. S. Nair, S. Mukherjee, N. Kachappilly, B. Pathak and S. Mandal, Gold Deassembly: From Au_{44}(SPh-(t)Bu)$_{28}$ to Au_{36}(SPh-(t)Bu)$_{24}$ Nanocluster through Dynamic Surface Structure Reconstruction, *J. Phys. Chem. Lett.*, 2021, **12**, 10987–10993.
29 C. Zhu, T. Duan, H. Li, X. Wei, X. Kang, Y. Pei and M. Zhu, Structural determination of a metastable Ag_{27} nanocluster and its transformations into Ag_8 and Ag_{29} nanoclusters, *Inorg. Chem. Front.*, 2021, **8**, 4407.
30 M. Lucarini and L. Pasquato, ESR spectroscopy as a tool to investigate the properties of self-assembled monolayers protecting gold nanoparticles, *Nanoscale*, 2010, **2**, 668–676.
31 E. S. Shibu, M. A. H. Muhammed, T. Tsukuda and T. Pradeep, Ligand Exchange of $Au_{25}SG_{18}$ Leading to Functionalized Gold Clusters: Spectroscopy, Kinetics, and Luminescence, *J. Phys. Chem. C*, 2008, **112**, 12168–12176.
32 R. Guo, Y. Song, G. Wang and R. W. Murray, Does Core Size Matter in the Kinetics of Ligand Exchanges of Monolayer-Protected Au Clusters, *J. Am. Chem. Soc.*, 2005, **127**, 2752–2757.
33 A. C. Templeton, W. P. Wuelfing and R. W. Murray, Monolayer-Protected Cluster Molecules, *Acc. Chem. Res.*, 2000, **33**, 27–36.
34 C. Zeng, C. Liu, Y. Pei and R. Jin, Thiol Ligand-Induced Transformation of $Au_{38}(SC_2H_4Ph)_{24}$ to Au_{36}(SPh-t-Bu)$_{24}$, *ACS Nano*, 2013, **7**, 6138–6145.
35 M. P. Maman, A. S. Nair, H. Cheraparambil, B. Pathak and S. Mandal, Size Evolution Dynamics of Gold Nanoclusters at an Atom-Precision Level: Ligand Exchange, Growth Mechanism, Electrochemical, and Photophysical Properties, *J. Phys. Chem. Lett.*, 2020, **11**, 1781–1788.
36 J. Wang, Z.-Y. Wang, S.-J. Li, S.-Q. Zang and T. C. W. Mak, Carboranealkynyl-Protected Gold Nanoclusters: Size Conversion and UV/Vis–NIR Optical Properties, *Angew. Chem., Int. Ed.*, 2021, **60**, 5959–5964.
37 M. G. Taylor and G. Mpourmpakis, Rethinking Heterometal Doping in Ligand-Protected Metal Nanoclusters, *J. Phys. Chem. Lett.*, 2018, **9**, 6773–6778.

38 G. Soldan, M. A. Aljuhani, M. S. Bootharaju, L. G. AbdulHalim, M. R. Parida, A.-H. Emwas, O. F. Mohammed and O. M. Bakr, Gold Doping of Silver Nanoclusters: A 26-Fold Enhancement in the Luminescence Quantum Yield, *Angew. Chem., Int. Ed.*, 2016, **55**, 5749–5753.
39 K. Kwak and D. Lee, Electrochemistry of Atomically Precise Metal Nanoclusters, *Acc. Chem. Res.*, 2019, **52**, 12–22.
40 J. Yan, H. Su, H. Yang, S. Malola, S. Lin, H. Häkkinen and N. Zheng, Total Structure and Electronic Structure Analysis of Doped Thiolated Silver $[MAg_{24}(SR)_{18}]^{2-}$ (M = Pd, Pt) Clusters, *J. Am. Chem. Soc.*, 2015, **137**, 11880–11883.
41 X. Lin, K. Sun, X. Fu, X. Ren, Y. Yang, C. Liu and J. Huang, Correlating Kernel–Shell Structures with Optical Properties of Pt_1Ag_{24} and Pt_1Ag_{14} Nanoclusters, *J. Phys. Chem. C*, 2021, **125**, 2194–2201.
42 X. Lin, X. Fu, Y. Yang, X. Ren, J. Tang, C. Liu and J. Huang, Synthesis and Optical Properties of Unique Pt_1Ag_{24} Nanoclusters with Mixed Exterior Motif Structures, *Inorg. Chem.*, 2021, **60**, 10167–10172.
43 X. Kang, M. Zhou, S. Wang, S. Jin, G. Sun, M. Zhu and R. Jin, The tetrahedral structure and luminescence properties of Bi-metallic $Pt_1Ag_{28}(SR)_{18}(PPh_3)_4$ nanocluster, *Chem. Sci.*, 2017, **8**, 2581–2587.
44 X. Kang, S. Jin, L. Xiong, X. Wei, M. Zhou, C. Qin, Y. Pei, S. Wang and M. Zhu, Nanocluster growth via "graft-onto": effects on geometric structures and optical properties, *Chem. Sci.*, 2020, **11**, 1691–1697.
45 H. Shen and T. Mizuta, An Alkynyl-Stabilized Pt_5Ag_{22} Cluster Featuring a Two-Dimensional Alkynyl–Platinum "Crucifix Motif", *Chem. – Eur. J.*, 2017, **23**, 17885–17888.
46 H. Shen and T. Mizuta, An Atomically Precise Alkynyl-Protected $PtAg_{42}$ Superatom Nanocluster and Its Structural Implications, *Chem. – Asian J.*, 2017, **12**, 2904–2907.
47 X. Kang, X. Wei, S. Wang and M. Zhu, Controlling the Phosphine Ligands of $Pt_1Ag_{28}(S\text{-}Adm)_{18}(PR_3)_4$ Nanoclusters, *Inorg. Chem.*, 2020, **59**, 8736–8743.
48 X. Kang and M. Zhu, Tailoring the photoluminescence of atomically precise nanoclusters, *Chem. Soc. Rev.*, 2019, **48**, 2422–2457.
49 C. Adamo and V. Barone, Toward reliable density functional methods without adjustable parameters: The PBE0 model, *J. Chem. Phys.*, 1999, **110**, 6158–6170.
50 F. Weigend and R. Ahlrichs, Balanced basis sets of split valence, triple zeta valence and quadruple zeta valence quality for H to Rn: Design and assessment of accuracy, *Phys. Chem. Chem. Phys.*, 2005, **7**, 3297–3305.
51 S. Grimme, J. Antony, S. Ehrlich and H. Krieg, A consistent and accurate ab initio parametrization of density functional dispersion correction (DFT-D) for the 94 elements H-Pu, *J. Chem. Phys.*, 2010, **132**, 154104.
52 E. Runge and E. K. U. Gross, Density-Functional Theory for Time-Dependent Systems, *Phys. Rev. Lett.*, 1984, **52**, 997–1000.
53 R. van Leeuwen, Causality and Symmetry in Time-Dependent Density-Functional Theory, *Phys. Rev. Lett.*, 1998, **80**, 1280–1283.
54 M. Frisch, G. Trucks, H. Schlegel, G. Scuseria, M. Robb, J. Cheeseman, G. Scalmani, V. Barone, G. Petersson, H. Nakatsuji, *et al.*, *Gaussian 16, Revision A.03*, Gaussian, Inc., Wallingford, CT, 2016.
55 T. Lu and F. Chen, Multiwfn: A multifunctional wavefunction analyzer, *J. Comput. Chem.*, 2012, **33**, 580–592.
56 Chemcraft-graphical software for visualization of quantum chemistry computations. **https://www.chemcraftprog.com**.
57 W. Sun, S. Jin, W. Du, X. Kang, A. Chen, S. Wang, H. Sheng and M. Zhu, Total Structure Determination of the $Pt_1Ag_9[P(Ph\text{-}F)_3]_7Cl_3$ Nanocluster, *Eur. J. Inorg. Chem.*, 2020, **6**, 590–594.
58 Y. Zhou, Y. Shen, J. Xi and X. Luo, Selective Electro-Oxidation of Glycerol to Dihydroxyacetone by PtAg Skeletons, *ACS Appl. Mater. Interfaces*, 2019, **11**, 28953–28959.
59 Q. Li, S. Yang, T. Chen, S. Jin, J. Chai, H. Zhang and M. Zhu, Structure determination of a metastable $Au_{22}(SAdm)_{16}$ nanocluster and its spontaneous transformation into $Au_{21}(SAdm)_{15}$, *Nanoscale*, 2020, **12**, 23694–23699.
60 Q. Yuan, X. Kang, D. Hu, C. Qin, S. Wang and M. Zhu, Metal synergistic effect on cluster optical properties: based on Ag_{25} series nanoclusters, *Dalton Trans.*, 2019, **48**, 13190–13196.

